Interfacial tension of the graphene-water solid-liquid interface: how to handle the electrostatic interactions?

Aziz Ghoufi, Patrice Malfreyt

To cite this version:

Aziz Ghoufi, Patrice Malfreyt. Interfacial tension of the graphene-water solid-liquid interface: how to handle the electrostatic interactions?. Molecular Physics, 2021, 119 (19-20), 10.1080/00268976.2021.1948121 . hal-03288474

HAL Id: hal-03288474
https://uca.hal.science/hal-03288474v1

Submitted on 16 Jul 2021

Interfacial tension of the graphene-water solid-liquid interface: how to handle the electrostatic interactions?

Aziz Ghoufi [a] and Patrice Malfreyt [b]

[a] Université Rennes, CNRS, Institut de Physique de Rennes (IPR) - UMR 6251, F-35000 Rennes, France
[b] Université Clermont Auvergne, CNRS, SIGMA Clermont, Institut de Chimie de Clermont-Ferrand (ICCF), F-63000 Clermont-Ferrand, France

ARTICLE HISTORY
Compiled June 16, 2021

ABSTRACT

We report molecular simulations of different graphene-water interfaces. Our aim is to calculate the interfacial tension as accurately as possible for a reasonable computational time by tuning on the value of the cut-off radius and the way of calculating the electrostatic interactions. We focus on the structure of water close to the graphene surface and on the profile of the interfacial tension along the direction normal to the surface. We then compare the Ewald summation method with two versions of the Reaction Field technique in different graphene interfaces.

KEYWORDS
Interfacial tension, reaction field method, graphene-water interface

1. Introduction

The calculation of the surface tension (γ) of liquid-vapour and liquid-liquid interfaces by molecular simulations [1–6] is under control in terms of dependencies of γ on methodological parameters [7] such as the interfacial area [8–10], the cutoff radius [11], the long-range corrections of the surface tension [12, 13] and the way of handling the electrostatic interactions [14]. Since most of the molecular simulations use a pair potential with a spherical cutoff at a distance r_c, long-range corrections must be added to the surface tension [7] to make up the missing part. It has been shown that this long-range contribution adequately compensates for the part coming from the truncated potential and that relatively small cutoff radii can be applied [11]. Actually, Figure 1 illustrates these dependencies by showing the different contributions of the surface tension with increasing cutoff values. From $r_c = 12$ Å, the total surface tension becomes nearly independent of the cutoff radius indicating that the long-range contributions to the surface tension effectively compensate for the effects of the Lennard-Jones potential truncation. Nevertheless, the intrinsic part due to the truncated potential shows a strong dependence on the cutoff by increasing from 8 to 12 mN m^{-1} as r_c is changing from 10 to 24 Å. We should point out that the long-range correction to the surface tension contributes much less in the surface tension

---

CONTACT Patrice Malfreyt . Email: Patrice.Malfreyt@uca.fr

when strong electrostatic interactions are involved in the system. For instance, at 298 K, this long-range correction represents only 10% of the surface tension of water [3] compared to 30% of the surface tension of Lennard-Jones (LJ) fluids.

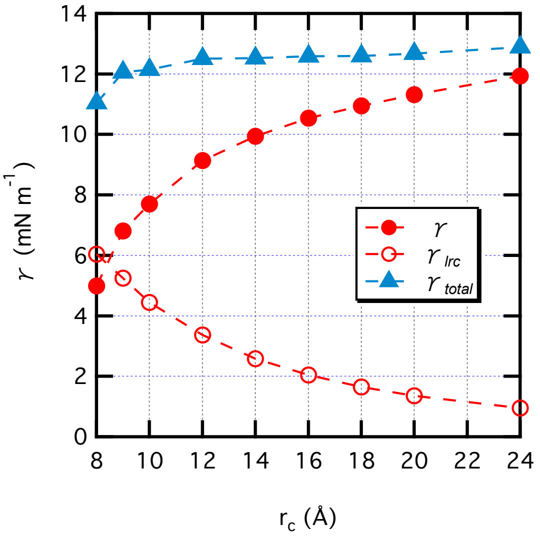

Figure 1. Liquid-vapour surface tensions of methane calculated at 125 K for different cutoff values. The long-range corrections (γ_{lrc}) to the surface are calculated using the local Janeček approach[13, 15] and the short range part γ using the Irving-Kirkwood definition [16, 17]. The total surface tension γ_{total} sums then γ_{lrc} and γ.

The methodological progress is far from being the same for solid-fluid interfaces [18, 19]. For the calculation of the solid-liquid interfacial tension, the impact of some of the factors mentioned above is still unknown. Concerning the long-range corrections to the interfacial tension of the graphene-methane interface modeled only with Lennard-Jones interactions, we have established that these tail corrections were negligible with respect to the intrinsic contribution even with a small cutoff value ($r_c = 12$ Å) [20, 21]. Does it mean that the choice of the cutoff radius will have no impact on the calculation of the intrinsic part of the interfacial tension of solid-liquid interfaces for truncated potentials ? What happens when electrostatic interactions coexist with LJ interactions ? We propose to answer these questions in this paper. In addition, depending of the geometry and nature of the solid surface, the calculation can become much more difficult because the internal stresses in the solid [22] has to be calculated. In the case of the graphene sheet immersed immersed in methane [20, 23] and water [21], it is possible to limit the calculation of the interfacial tension to that of the stress profile provided that the graphene is considered rigid. This is a reasonable approximation based on the extremely high values of Young's modulus and strength [24].

We recently calculated the interfacial tension of the graphene-water system [21]. The main conclusion of this work has been to show that the values of γ obtained from both the stress profile and the thermodynamic definition led to a contact angle value in agreement with recent experimental measurements [25]. From a methodological viewpoint, we have established the surface area dependence of the surface tension when the electrostatic interactions were calculated using both the Ewald summation (EW) method [26, 27] and the Reaction Field approaches [28, 29]. We need large dimension boxes to avoid any impact of the surface area on the interfacial tension leading to a dramatic increase in the computational time. One way to counteract this increase in computational cost due to the calculation in the reciprocal space is to use less expensive methods for the calculation of the electrostatic interactions such as the Reaction Field (RF) methods.

Actually, the calculation of electrostatic interactions has led to numerous studies on the accuracy and reliability of the simulated properties as a function of the schemes used : Ewald summation [26, 30, 31],truncation of the Coulomb interaction at a cutoff distance r_c with or without reaction-field correction [28, 29, 31, 32]. Extending the calculation of the electrostatic interactions to heterogenous systems led to additional difficulties such as taking into account the periodic conditions in a two-dimensional geometry [27, 30] and developing the normal and tangential pressure component profiles in the direction normal to the interface for the different electrostatic contributions [27] within the Ewald scheme.

Our previous works aimed to establish the system-size at which we no longer observe size-effects [21, 23]. In this paper, we aim to investigate the effects of changing the cutoff radius on the graphene-water interfacial tensions as the calculation of the electrostatic interactions is performed with the Ewald method, Reaction Field (RF) [28] and a damped version of The Reaction Field (RFD) [29] methods. At the end, we should able to recommend a value of cutoff radius to be used with truncated potentials (Lennard-Jones and Coulomb interactions) in solid-liquid interfaces to approach the interfacial tension of the Ewald summation method. Our recommendations will apply to different graphene interfaces : a graphene monolayer, a double layer of graphene and a carbon nanotube. We also take the route of using a nonpolorizable model for the graphene because this model [33] has been successfully applied to investigate the structure of water at the interface [33, 34] and the interfacial tension [21]. Polarizable models [35, 36] have also been used to model the graphene but these models have shown some significant deviations [37] from experiments for the reproduction of the surface tension of water. Section 2 presents the potential models and describes the calculation of the solid-liquid interfacial tension by using a free energy perturbation technique. The calculation of the long-range correction to the solid-liquid interfacial tension is also discussed. Section 3 discusses the impact of the cutoff radius of the structure and the shape of the profiles of the local tension of a graphene monolayer. We develop this section by the study of a bilayer of graphene and a carbon nanotube. In the conclusion, we give a recommandation of the use of the RFD method in the solid-liquid interfacial systems.

2. Potential models and methods

2.1. Potential

The total configurational energy U is the sum of intramolecular (U_{INTRA}) and intermolecular (U_{INTER}) energy contributions. The intermolecular contributions sum the repulsion-dispersion and electrostatic energies.

The graphene sheet was kept rigid with no intramolecular and intermolecular interactions between the atoms of graphene. The distance $C-C$ was fixed to 1.418 Å. Water is modeled using the four-point (TIP4P/2005) model [38] with no intramolecular interactions. The graphene sheet is formed by 2508 carbon atoms leading to a surface area $A = L_x L_y$ where $L_x = 81.05$ Å and $L_y = 80.83$ Å. The L_z dimension is then equal to 101.5 Å with 21400 water molecules in the simulation cell (see Figure

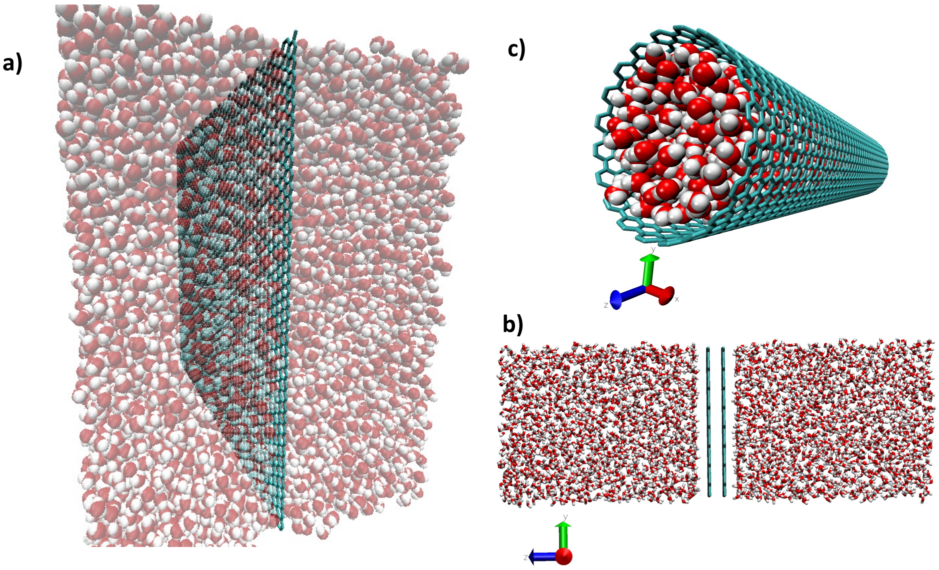

Figure 2. Typical configurations of a) a graphene monolayer layer, b) a graphene bilayer and c) a carbon nanotube (CNT) in interaction with water molecules at 300K where the $z-$direction is normal to the graphene surface for planar interfaces.

1). These box dimensions were selected from a previous study [21] in order to avoid any dependence of the interfacial tension on the surface area and to investigate only the dependence of the cutoff radius on truncated LJ and electrostatic interactions.

Since $U_{\text{INTRA}} = 0$ for water and graphene, the total energy of the system becomes

$$U = U_{\text{INTER}} = U_{LJ} + U_{ELEC} \tag{1}$$

It results from the definition of the system and the models used that only intermolecular interactions take place on the one hand between the water molecules and on the other hand between water molecules and carbon atoms of the graphene sheet. The intermolecular interactions due to the repulsion-dispersion interactions are computed using the truncated Lennard-Jones (LJ) potential

$$U_{LJ} \quad = \quad \sum_{i=1}^{N-1} \sum_{j>i}^{N} \sum_{a=1}^{N_i} \sum_{b=1}^{N_j} 4\epsilon_{ab} \left[\left(\frac{\sigma_{ab}}{r_{iajb}} \right)^{12} - \left(\frac{\sigma_{ab}}{r_{iajb}} \right)^{6} \right] \tag{2}$$

where r_{iajb} is the distance between atom a in molecule i and atom b in molecule j, ϵ_{ab} is the energy parameter of the interaction and σ_{ab} is the Lennard-Jones core diameter. N_i is the number of atoms in the molecule i. The LJ parameters for the graphene atom [39] are $\sigma = 3.3997$ Å and $\epsilon = 0.3594$ kJ mol^{-1}. The potential parameters including values of σ , ϵ for the water model can be found in the original paper [38]. The LJ parameters for the interactions between unlike sites are calculated by using the Lorentz-Berthelot combining rules.

The total electrostatic potential was calculated using both the Ewald sum method [26, 40] and the Reaction Field method [28]. For a box with orthogonal axes, the electrostatic energy calculated with the Ewald method is written as

$$\begin{aligned} U_{\mathrm{EW}} &= \frac{1}{2\epsilon_o V}\sum_{\mathbf{h}\neq 0} Q(h)S(\mathbf{h})S(-\mathbf{h}) \\ &+ \frac{1}{8\pi\epsilon_o}\sum_i\sum_a\sum_{j\neq i} q_{ia}\sum_b \frac{q_{jb}}{r_{iajb}}\ \mathrm{erfc}\ (\alpha r_{iajb}) \\ &- \frac{\alpha}{4\pi^{3/2}\epsilon_o}\sum_i\sum_a q_{ia}^2 \\ &- \frac{1}{8\pi\epsilon_o}\sum_i\sum_a\sum_{b\neq a}\frac{q_{ia}q_{ib}}{r_{iaib}}\mathrm{erf}\ (\alpha r_{iaib}) \qquad (3) \end{aligned}$$

where erfc(x) is the complementary error function and erf(x) is the error function. α is chosen so that only pair interactions in the central cell need to be considered in evaluating the second term in Eq.3. The functions $S(\mathbf{h})$ and $Q(h)$ are defined using Eqs.(4) and (5), respectively

$$S(\mathbf{h}) = \sum_i\sum_a q_{ia}\exp(i\mathbf{h}.\mathbf{r_{ia}}) \qquad (4)$$

$$Q(h) = \frac{1}{h^2}\exp(-\frac{h^2}{4\alpha^2}) \qquad (5)$$

where the reciprocal lattice vector $\mathbf{h}$ is defined as $\mathbf{h} = 2\pi(l/L_x, m/L_y, n/L_z)$ where l, m, n take values of 0,±1,±2,$\cdots \pm\infty$. The final term in Eq.3 is a compensation term that consists of removing terms corresponding to the potential energy of an ion a due to the gaussian charge on a neighbouring charge b (or vice versa).

With the Reaction Field (RF) method proposed by Neumann [28], the electrostatic energy is calculated as follows

$$U_{\mathrm{RF}} = \frac{1}{8\pi\epsilon_o}\sum_i\sum_a\sum_{j\neq i}\sum_{b\neq a} q_{ia}q_{jb}\times\left[\frac{1}{r_{iajb}} + \frac{B_0 r_{iajb}^2}{2r_c^3} - \frac{1}{r_c} - \frac{B_0}{2r_c}\right] \qquad (6)$$

In the Damped Reaction Field (RFD) version [29], the reaction term is modified by using a distance depending function that is identical to that used in the real-space term of the Ewald sum. The electrostatic energy in the RFD approach becomes then

$$\begin{aligned} U_{\mathrm{RFD}} = \frac{1}{8\pi\epsilon_o}\sum_i\sum_a\sum_{j\neq i}\sum_{b\neq a} q_{ia}q_{jb} \quad & \Bigg[\left(\frac{\mathrm{erfc}(\alpha r_{iajb})}{r_{iajb}} + \left(\frac{\mathrm{erfc}(\alpha r_c)}{r_c^2} + \frac{2\alpha}{\sqrt{\pi}}\frac{\exp(-\alpha^2 r_c^2)}{r_c}\right) r_{iajb}\right) \\ & - \left(\frac{\mathrm{erfc}(\alpha r_c)}{r_c} + \left(\frac{\mathrm{erfc}(\alpha r_c)}{r_c^2} + \frac{2\alpha}{\sqrt{\pi}}\frac{\exp(-\alpha^2 r_c^2)}{r_c}\right) r_c\right) \qquad (7) \\ & + \frac{B_0(r_{iajb}^2 - r_c^2)}{2r_c^3}\Bigg] \qquad (8) \end{aligned}$$

where B_0 is defined as

$$B_0 = \frac{2(\epsilon_1 - 1)}{2(2\epsilon_1 + 1)} \tag{9}$$

ϵ_1 is the dielectric constant outside the cavity. For water [41], we take $\epsilon_1 = 78.5$.

2.2. Methods

The molecular dynamics (MD) simulations were carried out with the DL_POLY package [42] by using the Velocity-Verlet scheme [26] to integrate the equations of motion. The simulations were carried out in the $\mathrm{N}p_\mathrm{N}\mathrm{AT}$ statistical ensemble where the normal component of the pressure $p_\mathrm{N} = p_{zz}$ was fixed to 1 bar. The area of the graphene surface is represented by A. The temperature T was fixed to 300 K. We applied the Hoover [43] thermostat and barostat with relaxation times of $\tau_t = 0.5$ ps and $\tau_p = 0.1$ ps. The simulations of the carbon nanotube were performed in the canonical NVT ensemble.

The MD simulations were performed with a time step of 1 fs over an equilibration period of 10 ns. The thermodynamic and structural properties were averaged over an acquisition phase of 10 ns. The Lennard-Jones potential and the electrostatic interactions were truncated at r_c ranging from 12 to 16 Å. The long-range electrostatic interactions, handled using the Ewald summation technique, were calculated within a relative error of 10^{-6}. α was taken to 0.2365 Å^{-1}. Statistical fluctuations of interfacial tensions were estimated using the variation in the block averages. The statistical fluctuations are shown in Figure A1 of Appendix A for the calculation of the local surface tension.

2.3. Solid-liquid interfacial tension

The interfacial tension, calculated in the constant NVT-ensemble, is expressed through the thermodynamic definition of $\gamma = \left(\frac{\partial F}{\partial A}\right)_{N,V,T}$ where F is the free energy, A the surface area, N the number of molecules and V the volume. we take the route of using the non-exponential method [5] based on the test-area methodology [44] where γ is expressed as $\gamma = \left(\frac{\partial F}{\partial A}\right)_{N,V,T}$ with F the free energy, A the surface area, N the number of molecules and V the volume. This non-exponential method was recently developed from a rigorous theoretical background [5]. The surface tension becomes

$$\begin{aligned}
\gamma_\mathrm{TA} &= \left(\frac{\partial F}{\partial A}\right)_{N,V,T} = \lim_{\xi \to 0} \left\langle \left(\frac{(U^{(1)}(\mathbf{r}'^N) - U^{(0)}(\mathbf{r}^N))}{\Delta A} \right) \right\rangle_0 \\
&= \lim_{\xi \to 0} \left\langle \left(\frac{(U^{(1)}(\mathbf{r}'^N, \xi) - U^{(0)}(\mathbf{r}^N))}{A\left[(1 \pm \xi)^{-1/2} - 1\right]} \right) \right\rangle_0
\end{aligned} \tag{10}$$

where $\mathbf{r}^N$ is the set of Cartesian coordinates $\mathbf{r}_i$ of each molecular centre of mass in the system and $\mathbf{r}'^N$ the set of modified Cartesian coordinates which are scaled as in

Eq.11 in the perturbed state:

$$\left\{ \begin{array}{lll} x_i \longrightarrow x'_i = & x_i\sqrt{1 \pm \xi} \\ y_i \longrightarrow y'_i = & y_i\sqrt{1 \pm \xi} \\ z_i \longrightarrow z'_i = & z_i(1 \pm \xi)^{-1} \end{array} \right. \tag{11}$$

$U^{(0)}(\mathbf{r}^N)$ and $U^{(1)}(\mathbf{r'}^N)$ are the configurational energies of the reference and perturbed states. The difference in the surface area ΔA is $A^1 - A^0$ where 0 stands for the reference state and 1 stands for the perturbed state. The anisotropic transformations were used $L^{(1)}_{x,y} = L^{(0)}_{x,y}\sqrt{1 \pm \xi}$, and $L^{(1)}_z = L^{(0)}_z/(1 \pm \xi)$ where ξ is the perturbation length as $\xi \to 0$ and L the box length. The area of a planar interface is $A = 2L_xL_y$ and $\Delta A = A\left[(1 \pm \xi)^{-1/2} - 1\right]$.

A local version of Eq.C1 was obtained by assuming the decorrelation of slabs [45]

$$\gamma_{\mathrm{TA}}(z) = \lim_{\xi \to 0} \left\langle \sum_{i=1}^{N} \sum_{j=i+1}^{N} H(z_i - z, \Delta z) \left(\frac{(u^{(1)}_z(\mathbf{r'}_{ij}, \xi) - u^{(0)}_z(\mathbf{r}_{ij}))}{\Delta A} \right) \right\rangle_0 \tag{12}$$

where u_z is the energy of the slab located at z, $\mathbf{r}_{ij}$ is the distance between i and j molecules, $\mathbf{r'}_{ij}$ is calculated in the perturbed state by using the scaling of Eq.11. $H(z_i)$ is the top-hat function defined by

$$H(z_i - z, \Delta z) = \left\{ \begin{array}{ll} 1 & \text{for } z - \frac{\Delta z}{2} < z_i < z + \frac{\Delta z}{2} \\ 0 & \text{otherwise} \end{array} \right. \tag{13}$$

Interfacial tension is thus be evaluated by

$$\gamma_{\mathrm{TA}} = \frac{1}{2} \sum_{k}^{N_s} \gamma_{\mathrm{TA}}(z_k) \tag{14}$$

where N_s is the number of slabs of volume $V_s = L_xL_y\Delta z$ and Δz the slab thickness. In the case of the monolayer of graphene, the simulation box is divided into $N_s = 500$ slabs of thickness $\Delta z = 0.24$ Å. The factor 1/2 is introduced in order to take into account that the system considers two interfaces.

When the interface tension is calculated in Np_{N}AT statistical ensemble, its operational expression is then established in Appendix B. The additional term $< p_{\mathrm{N}}L_z >$ contributes by about 1 mN m^{-1} to the total interface tension. For the calculation in cylindrical geometries, the operational expression of γ and the methodology are described in Appendix C.

The long-range correction to the surface tension in the TA approach is calculated by considering the Lennard-Jones contribution. The tail correction of the surface tension within the test-area formalism is then approximated by

$$\begin{aligned}\gamma_{\mathrm{TA,LRC}} &= \sum_{k}^{N_s} \lim_{\xi \to 0} \left\langle \left(\frac{(u_{\mathrm{LRC}}^{(A+\Delta A)}(z_k')) - (u_{\mathrm{LRC}}^{(A)}(z_k))}{\Delta A} \right) \right\rangle_0 \\ &= \sum_{k}^{N_s} \gamma_{\mathrm{LRC}}(z_k) \qquad (15)\end{aligned}$$

where

$$u_{\mathrm{LRC}}(z_k) = \pi \rho(z_k) V_s \sum_{i=1}^{N_C} \sum_{j=1}^{N_C} x_i(z_k) \int_{r_c}^{\infty} dr \int_{-r}^{r} d\Delta z \left[\rho_j(z) - \rho_j(z_k)\right] \; r \; U_{\mathrm{ij,LJ}}(r) \qquad (16)$$

where $\rho_j(z_k)$ is the density number of the species j in the slab k, respectively. $x_i(z_k)$ and $x_j(z_k)$ are the mole fractions of molecular species i and j in the slab k. N_C is the number of molecular types in the system, here $N_C = 2$. Δz is defined as the difference $z - z_k$ and varies between $-r$ and r. When a molecule located at z_k is selected as the central molecule, z_k will be constant. r_c is the cutoff radius, $U_{\mathrm{ij,LJ}}(r)$ is the intermolecular Lennard-Jones energy with r being the distance between the two centers of mass of molecules of species i and j.

$$U_{\mathrm{ij,LJ}}(r) = \sum_{a}^{N_i} \sum_{b}^{N_j} 4\epsilon_{ab} \left[\left(\frac{\sigma_{ab}}{r} \right)^{12} - \left(\frac{\sigma_{ab}}{r} \right)^{6} \right] \qquad (17)$$

The corresponding tail corrections calculated in cylindrical geometries are given in Appendix C. We report in Figure 3 the local long-range corrections to the interfacial tension of the graphene-water interface at different cutoff radii. The total contribution, obtained by summing the local values, is read as the asymptotic value on the right axis. This tail contribution increases from (-2.1 to 0.11) ±0.1 mN m^{-1} as r_c is changing from 12 to 16 Å. The sign of this long-range contribution is negative in contrast to the same contributions calculated for liquid-vapour and liquid-liquid interfaces [7]. However, the absolute value of this long-range correction decreases with increasing cutoff values as expected for a correction of the truncated LJ potential. We conclude that this tail correction is negligible within the statistical fluctuations with respect to the intrinsic part for the geometries and types of interactions investigated in this paper.

3. Results and discussions

4. Interaction of water with a monolayer of graphene

The system is formed by a graphene sheet surrounded by two reservoirs of water molecules. We define here the graphene surface as a two dimensional planar material made up of a monolayer of carbon atoms. The carbon atoms are placed in a hexagonal honeycomb lattice, located at $z = 0$. The structure of the graphene-water interface is investigated through the center of mass density profiles of water molecules calculated

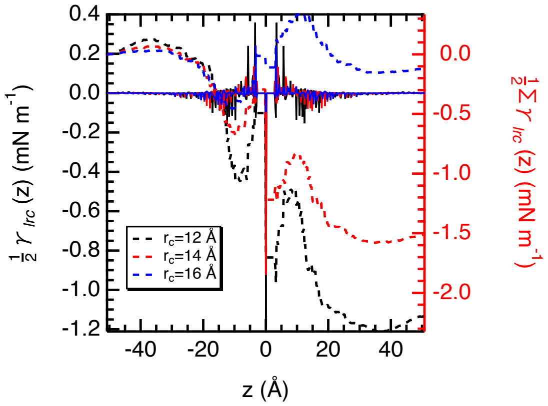

Figure 3. Profiles of the long-range corrections to the interfacial tension of the graphene-water interface calculated using Eq.15 at different cutoffs. The total interfacial tension is the last value read on the right-hand axis.The statistical fluctuations of the long-range corrections are about 0.01 mN m^{-1} for the graphene-water interface.

along the z-direction normal to the interface. The profiles, shown in Figure 4(a), were calculated with the EW, RF and RFD methods with a cutoff radius of 12 Å. The interaction of the water molecules with the graphene sheet leads to a layered structure that is characterized by three peaks of decreasing magnitudes. The height of the first peak is about 3000 kg m^{-3} whereas the height of the second is about half of the first peak. The bulk water density is recovered at about 12 Å from the graphene sheet. On the scale of Figure 1, the different methods used for the calculation of the electrostatic interactions lead to the same layered organization of water molecules in terms of heights and locations of the adsorption peaks.

Figure 4(b) shows the profiles of the local interfacial tension $\gamma(z)$ along the direction normal to the graphene sheet. The interfacial tension was calculated with the test-area (TA) method with a local operational expression described in a previous paper [21]. The interfacial tensions, obtained by summing the local values over all the slabs, are given in Table 1. The analysis of the curves shown that the interfacial tension results from integration of peaks from 0 to 12 Å. Beyond this distance from the surface, the local surface tension has converged and we observe no contributions of water molecules to this property. Some differences appear in the magnitude of the peaks of $\gamma(z)$ depending on the method used for the calculation of the electrostatic interactions. Later, we will investigate later the differences in $\gamma(z)$ in the water region as a function of the method and the cutoff used.

The values of interfacial tensions are given in Table 1 for three different cutoff values. The interfacial tension calculated with the Ewald method with a cutoff radius of 12 Å will serve as a basis for comparison. First, we can deduce from Table 1 that the cutoff radius has a very little impact on the interfacial tension calculated with either RF or RFD. The variations of the interfacial tension with the cutoff are within the standard deviations. We only observe that the values calculated with RF And RFD are slightly smaller ($< 3\%$) than that calculated with Ewald. The simulated interfacial tensions with RF and RFD range from 95.2 to 97.9 mN m^{-1} and correspond to a contact angle of about 75^o in a very good agreement wit the recent experimental measurement of this angle ($\theta_{\rm exp.} = 71^o$) [25].

The decomposition of the interfacial tension into the LJ and electrostatic contributions is shown in Figure D1 of Appendix D. The electrostatic contribution is about 576

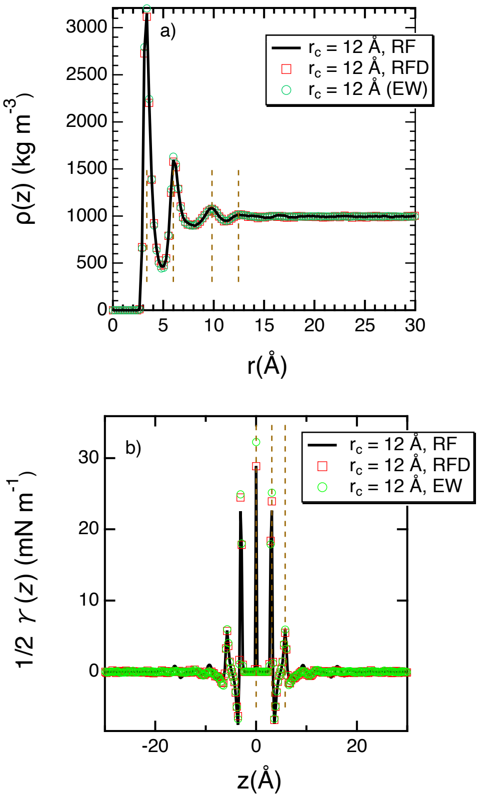

Figure 4. a) Center of mass density profiles of water molecules calculated along the direction normal to the graphene surface with a cutoff radius of 12 Å and three different methods (RF, RFD, EW) for the treatment of the electrostatic interactions. We focus on only one interface; b) Profiles of the local surface tension $\gamma(z)$ calculated with the test-area (TA) approach depending on how the electrostatic interactions are calculated (see Ref. [21] for a description of the operational expression of the interfacial tension $\gamma(z)$). The profiles are shown for the two graphene-water interfaces. The vertical dotted lines show the z-positions of the different peaks.

mN m^{-1} whereas the LJ part contributes negatively to -479.7 mN m^{-1}. This strong negative part of the interfacial tension of the LJ contribution is the result of positive interactions between LJ centers which interact on average at a smaller distance smaller than the LJ particle diameter. For example, in the case of the liquid-vapour interface of water, the LJ part to the surface tension is about -245 mN m^{-1} for a surface tension of 72 mN m^{-1}. The stronger negative value calculated in the solid-liquid interface indicates that the water molecules are more associated and structured when they interact with the solid in line with the layering of water molecules (see Figure 4(a)). The water molecules approaching the graphene surface arrange to form a two-dimensionally hydrogen bond network to compensate for the break in symmetry on the side of graphene.

Figures 5(a) and 5(c) show the molecular density profiles of water molecules calculated with the RF and RFD methods for different cutoff radii. The curves are represented with a scale adapted to the variations in the liquid phase. The density profile calculated with the Ewald method at $r_c = 12$ Å is given for comparison. The profile calculated with Ewald is much less noisy than those obtained with RD and RFD techniques. In addition, we observe that the value of the cutoff radius does not impact on the shape of the density profiles. The impact of the method used, RF or RFD, does

Table 1. Values of the graphene-water interfacial tensions calculated in different geometries with the Ewald (EW), Reaction Field (RD) and Damped Reaction Field (RFD) methods at three different cutoffs (r_c). The subscripts give the accuracy of the last decimal(s), i.e., 99.0_{12} means 99.0±1.2 mN m^{-1}.

r_c (Å)	γ_{EW} (mN m^{-1})	γ_{RF} (mN m^{-1})	γ_{RFD} (mN m^{-1})
graphene monolayer - water interface			
12	99.0_{12}	96.5_{13}	96.3_{13}
14		95.2_{18}	97.9_{19}
16		95.7_{17}	96.7_{21}
graphene monolayer (flexible) - water interface			
12			92.6_{14}
graphene bilayer - water interface			
12	65.7_{20}	64.2_{30}	69.4_{15}
nanotube-water interface			
12	140.1_{26}	136.5_{41}	138.0_{32}

not result in significant changes in local densities. As a conclusion, the way of calculating the electrostatic interactions does not change the local structure of the water molecules along the direction normal to the graphene and no influence of the cutoff radius (from $r_c > 12$ Å) is shown on the structural properties.

Figures 5(b) and 5(d) show the profiles of the interfacial graphene-water interfacial tension calculated at different increasing cutoff radii with both RF and RFD techniques. First, we observe that changing the method of handling the electrostatic interactions from RF to RFD is equivalent to decreasing the oscillations of the local interfacial tension in the bulk phases. Actually, the fluctuations of the interfacial tension are halved with RFD with $\gamma = 0.003 \pm 0.15$ mN m^{-1} in the bulk water phase. The influence of the cutoff on the profiles of γ is not clearly established on Figures 5(b) and 5(d) regardless of the RF and RFD method. Very interestingly, we conclude from Figure 5(d) that the RFD method makes it possible to reproduce the profile calculated with the Ewald method assumed here as the reference method. The oscillations are significantly reduced with RFD compared to RF. Actually, the fact that these oscillations remain greater for RF originates from the strong correlations due to the Coulombic interactions at short distances and the use of a damped function $\frac{\mathrm{erfc}(\alpha r)}{r}$ instead of $\frac{1}{r}$ which ensures faster convergence. When the long-range interactions are explicitly calculated with Ewald or emulated with RFD, these correlations disappear and the profiles become smoother. Since the RFD method is twice as fast as the Ewald technique, the simulation of the solid-liquid interface could be done with the RFD method to obtain accurate local structure and interfacial tension profiles.

We complete the study of the interface of water with a single layer of graphene by considering a fully flexible graphene interface. The flexibility of the graphene is considered by the Tersoff potential [23]. We do not observe any differences in the local ordering with the nature of the interface as shown in Figure 6(a). The profiles of the interfacial tensions do not show any significant different at this scale. The interfacial tension calculated with the RFD method is slightly smaller with a flexible sheet (92.6 mN m^{-1}) compared to that of a static layer of graphene (96.3 mN m^{-1}, see Table 1) but it remains within the range of statistical uncertainty.

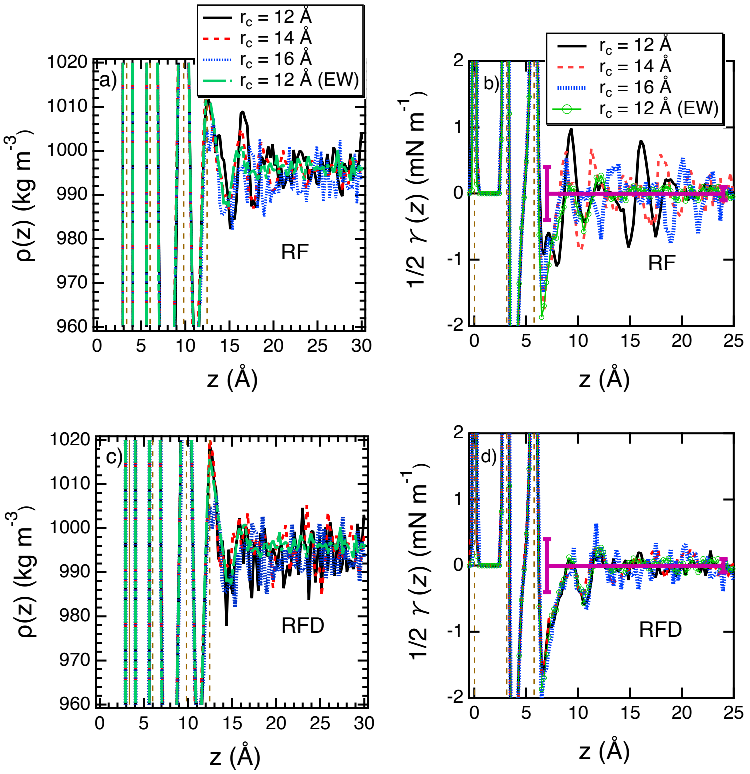

Figure 5. Molecular density profiles of the water molecules in the direction normal to the graphene sheet calculated at different cutoff values with the a) RF and b) RFD techniques. The vertical dotted lines show the z-positions of the peaks in the density profiles as shown in Figure 4(a); Local interfacial tension profiles between the c) RF, d) RFD methods calculated at different cutoff radii. The density and surface tension profiles calculated with the Ewald (EW) summation technique are shown for comparison. The statistical fluctuations calculated as a function of z (see Figure A1) are shown at two typical z-positions, $z = 7$ and 24 Å in b) and d).

5. Interaction of water with a bilayer of graphene

We now turn our attention to the transferability of the method to another geometry. We investigate then a structure formed by two layers of graphene. The distance between the graphene sheets was fixed to 3.32 Å. Figure 7(a) shows the molecular density profiles of water along the z-direction for a single and a double layer of graphene calculated with the RFD approach. First, we show that the presence of a second layer of graphene does not change the layering of water molecules close to the surface with respect to a monolayer. The description of the local interface tension with the bilayer of graphene is similar with RDF and Ewald methods. The simulated interfacial tension, given in Table 1, shows a significant decrease in this property of about 27 mN m^{-1} when duplicating the number of graphene layers. We obtain a reasonable agreement between the different methods EW, RF and RFD on the calculation of γ taking into account the statistical fluctuations. Given the geometry of the system, the negative contribution provided by the presence of the second layer can be explained by less attractive interactions between the water molecules of the two reservoirs on either side of the graphene due to the increasing separation distance. The contact angle of water should then increase with the number of layers [46].

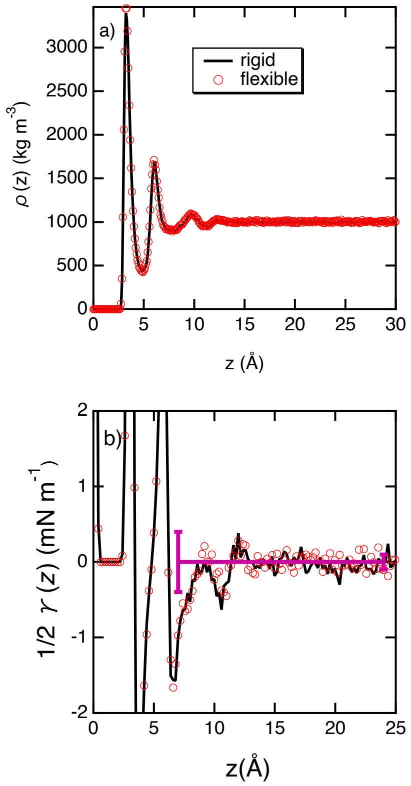

Figure 6. a) Water density and b) interfacial tensions profiles calculated with a static and flexible graphene sheet by using the RFD method and $r_c = 12$ Å. The statistical fluctuations calculated as a function of z (see Figure A1) are shown at two typical z-positions, $z = 7$ and 24 Å in b).

6. Confinement of water in a carbon nanotube

We now focus on the molecular simulation of water molecules in a carbon nanotube formed by 3280 carbon atoms with a pore radius of 13.4 Å. The box dimension along the z-direction is fixed to 100.7 Å. The interfacial tensions profiles are calculated with operational expressions for cylindric geometries [47] (see Appendix C). The local density of water inside the carbon nanotube is described in the same way with RDF and EW methods suggesting that the RDF approach performs very well for confined systems. Both methods show an excellent agreement on the local values of the interfacial tension inside the pore. The total interfacial tension, reported in Table 1 is equal to 138, 136.5 and 140.1 mN m^{-1} for RFD, RF and EW, respectively. This large value of interfacial tension compared to those calculated in the planar geometries in this work is the result of strong confined and oriented water molecules [48]. Once again, the consistency of the interfacial tension calculation with RFD is demonstrated in relation to the one performed with EW.

7. Summary

We took the route of simulating a system-size at which no size-effects are observed. In order to reduce the prohibitive computational time with well-developed box dimen-

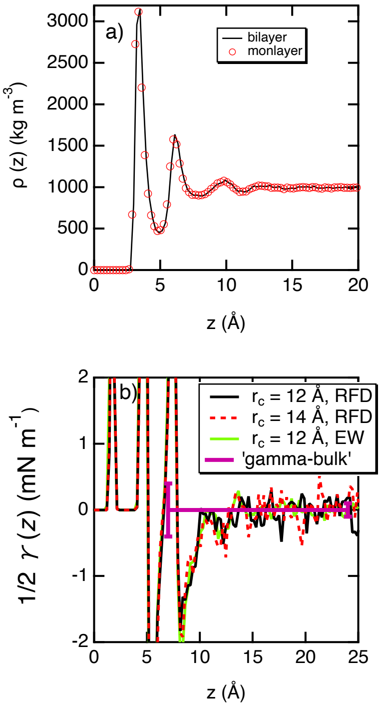

Figure 7. a) Molecular density profiles of water calculated in a monolayer and a bilayer of graphene by using the RFD method; b) profiles of interfacial tension calculated in a bilayer of graphene in water with the RFD and Ewald methods at different cutoff values as indicated in the legend. The statistical fluctuations calculated as a function of z (see Figure A1) are shown at two typical z-positions, $z = 7$ and 24 Å in b).

sions, alternatives are possible in the choice of the method for calculating electrostatic interactions. We did a comparison between truncated reaction field methods and the widely used Ewald summation method. We also aimed to check the impact of the choice of the cutoff radius on the calculation of the interfacial tension. The main result is that the intrinsic part of the interfacial tension does not show any dependence on the cutoff radius contrary to what has been shown in liquid-vapour interfaces. We conclude that the simulated graphene-water interfacial is in line with the experimental water contact angle irrespective of the method (RF, RFD, Ewald) used. In addition, we demonstrate here that the RFD technique leads to a profile of the interfacial tension with much less oscillations and therefore closer to the one calculated with the Ewald method. Finally, we recommend the use of the RFD method with a cutoff radius of 12 Å for the calculation of the electrostatic interactions in solid-liquid interfacial systems with both a good reproduction of the structure and interfacial tension with a computational cost reduced by half. Our conclusions apply to isotropic planar surfaces (static and flexible monolayer of graphene, a bilayer of graphene) and cylindric geometries.

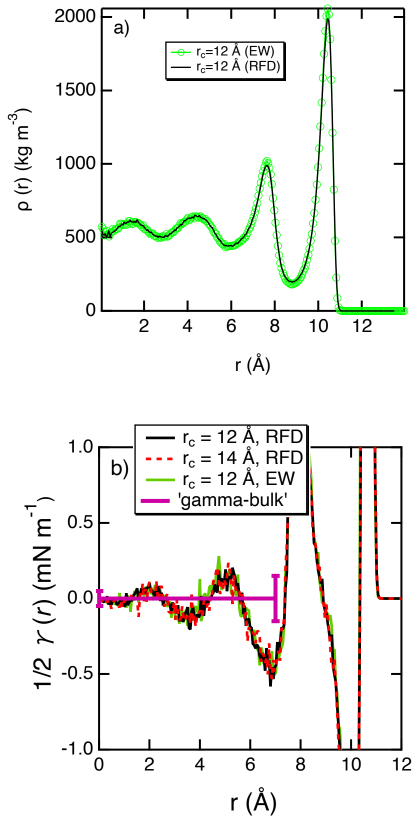

Figure 8. Profiles of the a) radial density of water molecules confined in the nanotube and b) interfacial tensions as a function of the radial distance r. The profiles are represented on half the boxlength. The statistical fluctuations calculated as a function of z (see Figure A1) are shown at two typical z-positions, $z = 0$ and 7 Å in b).

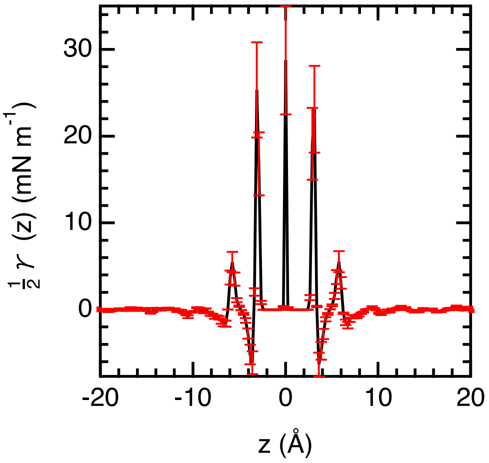

Figure A1. Profile of the surface tension (mN m^{-1}) of the graphene monolayer water interface along the z-dimension. The statistical fluctuations are represented by error bars calculated over 5 block-averages during the acquisition phase.

Appendix A. Statistical fluctuations calculated on the surface tension profiles

Appendix B. Operational expression of γ calculated with TA in the Np_{N}AT ensemble.

In a classical system constituted by N identical particles of mass m defined by their coordinates $\mathbf{r}^N$ and momenta $\mathbf{p}^N$, the Gibbs free energy G is related to the partition function $Q_{Np_{\mathrm{N}}AT}$ by the following expression

$$\begin{aligned} G &= -k_B T \ln Q_{Np_{\mathrm{N}}AT} && \text{(B1)} \\ &= -k_B T \ln \left(\frac{1}{\Lambda^{3N} N! V_o} \int \int d\mathbf{r}^N dV \exp \left(- \frac{U(\mathbf{r}^N) + p_{\mathrm{N}} V}{k_B T} \right) \right) && \text{(B2)} \end{aligned}$$

where V_o is an arbitrary unit of volume that makes the partition function dimensionless and $\mathbf{r}^N$ is the potential energy and p_{N} is the normal pressure of the system. Λ is the de Broglie thermal wavelength. The surface tension γ is defined as the thermodynamic derivative of the Gibbs free energy with respect to the interacial area A as

$$\gamma = \left(\frac{\partial G}{\partial A} \right)_{Np_{\mathrm{N}}AT} = -k_B T \frac{1}{Q} \left(\frac{\partial Q}{\partial A} \right)_{Np_{\mathrm{N}}AT} \tag{B3}$$

$$\gamma = \left\langle \left(\frac{\partial U(\mathbf{r}^N)}{\partial A} \right) + p_N \left(\frac{\partial V}{\partial A} \right) \right\rangle_{Np_{\mathrm{N}}AT} \tag{B4}$$

The calculation of the second term of the right-hand side of Eq.(B4) requires to express the derivative of the volume with respect to A according to

$$dV = L_z dA + A dL_z = \left(\frac{\partial V}{\partial A} \right)_{L_z} dA + \left(\frac{\partial V}{\partial L_z} \right)_A dL_z \tag{B5}$$

with

$$\left(\frac{\partial V}{\partial A} \right)_{L_z} = L_z \quad \text{and} \quad \left(\frac{\partial V}{\partial L_z} \right)_A = A \tag{B6}$$

The different partial derivatives relating the variables V, A and L_z obey to the following equation

$$\left(\frac{\partial V}{\partial A} \right)_{L_z} \cdot \left(\frac{\partial L_z}{\partial V} \right)_A \cdot \left(\frac{\partial A}{\partial L_z} \right)_V = -1 \tag{B7}$$

From Eq.(B7), it turns out that the derivative $\left(\frac{\partial V}{\partial A} \right)_A$ does not exist. It then follows that $\left(\frac{\partial V}{\partial A}\right)_A = 0$. The surface tension of Eq.(B4) becomes

$$\gamma_{Np_{\mathrm{N}}AT} = \left\langle \left(\frac{\partial U(\mathbf{r}^N)}{\partial A} \right)_A \right\rangle \tag{B8}$$

$$= \left\langle \left(\frac{\partial U(\mathbf{r}^N)}{\partial A} \right)_{L_z} + p_{\mathrm{N}} L_z \right\rangle \tag{B9}$$

$$= \lim_{\xi \to 0} \left\langle \left(\frac{(U^{(1)}(\mathbf{r'}^N, \xi) - U^{(0)}(\mathbf{r}^N))}{A\left[(1 \pm \xi)^{-1/2} - 1\right]} \right) + p_{\mathrm{N}} L_z \right\rangle_0 \tag{B10}$$

where the angular brackets denote an average over the $Np_{\mathrm{N}}AT$ ensemble.

Appendix C. Operational expression for the calculation of γ in cylindrical geometries

C.1. Calculation of the intrinsic part of the surface tension

The intrinsic part of the surface tension is calculated by using the non-exponential form [5] of the test-area (TA) method [44]. In this thermodynamic definition, γ_{I} is expressed as $\left(\frac{\partial F}{\partial A}\right)_{N,V,T}$ where F is the free energy, A the surface area N the number of molecules and V the volume. Calculation [2] of $\frac{\partial F}{\partial A}$ is performed from an explicit derivation $\gamma_{\mathrm{I}} = \left\langle \frac{\partial U}{\partial A} \right\rangle_{N,V,T}$ where U is the configurational energy. This expression is approximated through a finite difference such that $\gamma = \left\langle \frac{\partial U}{\partial A} \right\rangle_{N,V,T} = \left\langle \frac{\Delta U}{\Delta A} \right\rangle_{N,V,T}$ where ΔU is the difference of the energy between both states 0 and 1 characterized by surface areas A^0 and $A^0 \pm \Delta A$, respectively. Keeping the volume constant leads to the following anisotropic transformations: $L_\alpha^{(1)} = L_\alpha^{(0)}\sqrt{1 \pm \xi}$, with $\alpha = x$ or y and $L_z^{(1)} = L_z^{(0)}/(1 \pm \xi)$ where ξ is the perturbation length as $\xi \to 0$ and L the box length.

The area of a cylindrical interface is defined by $A = 2\pi R_e L_z$ and $\Delta A = A\left[(1 \pm \xi)^{-1/2} - 1\right]$, where R_{e} is the radius of the equimolar dividing surface. R_{e} is calculated from the radial density profile ($\rho(r)$) from $R_{\mathrm{e}}^2 = \frac{1}{\rho_v - \rho_l} \int_0^\infty r^2 \frac{d\rho(r)}{dr} dr$ where ρ_{v} and ρ_{l} are the vapor and liquid densities, respectively. This choice is arbitrary and other definitions are possible such as a fit of the density profile by using a hyperbolic tangent function. Therefore, the surface tension (γ_{I}) is given by

$$\gamma_{\mathrm{I}} = \left(\frac{\partial F}{\partial A} \right)_{N,V,T} = \lim_{\xi \to 0} \left\langle \left(\frac{(U^{(1)}(\mathbf{r'}^N) - U^{(0)}(\mathbf{r}^N))}{\Delta A} \right) \right\rangle_0 \tag{C1}$$

where $U^{(0)}(\mathbf{r}^N)$ and $U^{(1)}(\mathbf{r'}^N)$ are the configurational energies of the reference and perturbed states, respectively. $\mathbf{r}^N$ and $\mathbf{r'}^N$ are the configurational space for both states. $< ... >_0$ means that the average is performed over the reference state. A local version of Eq. (C1) can be obtained by assuming a decorrelation of the cylindrical slabs [50]

$$\gamma_{\mathrm{I}}(R_k) = \lim_{\xi\to 0} \left\langle \sum_{i=1}^{N}\sum_{j>i}^{N} H(R_{ik}) \left(\frac{(u_{R_k}^{(1)}(\mathbf{r}_{ij}) - u_{R_k}^{(0)}(\mathbf{r}_{ij}))}{\Delta A} \right) \right\rangle_0 \tag{C2}$$

where k is the index of the cylindrical slab, R_k the radius of the cylindrical shell, u_{R_k} is the energy of the kth element, $H(R_{ik})$ is the Heaviside function with $H(R_{ik}) = 1$ for $R_i = R_k$ and 0 otherwise and r_{ij} is the distance between molecules i and j.

C.2. Calculation of the long-range corrections to the surface tension

Since the operational expression of the TA method uses the configurational energy, the long-range corrections (LRC) to the energy are then used to build the tail corrections of the surface tension. Since we use the non-exponential form of the TA method for the calculation of the intrinsic part, we keep the same formalism for the calculation of the long-range corrections. Thus, the local LRC contribution of the surface tension (γ_{LRC}) can be expressed by

$$\begin{aligned} \gamma_{LRC}(R_k) &= \lim_{\xi\to 0} \left\langle \left(\frac{(u_{LRC}(R_k)^{(1)} - u_{LRC}(R_k)^{(0)})}{\Delta A} \right) \right\rangle_0, \\ \gamma_{LRC} &= \sum_k \gamma_{LRC}(R_k) \end{aligned} \tag{C3}$$

where $u_{LRC}(R_k)$ is the LRC energy of the kth element (R_k). For the configurational energy the local LRC for each molecule i can be expressed in spherical coordinates as

$$u_{i,LRC} = \frac{1}{2}\int_{r_c}^{\infty} dr \int_0^{\pi} d\theta \int_0^{2\pi} d\phi \rho(r) u(r) r^2 \sin\theta \tag{C4}$$

where the factor $\frac{1}{2}$ avoids a double accounting. For a system with a cylindrical interface, density and other properties change only in the radial direction to the interface. Thus, Eq. (C4) can be expressed as

$$u_{i,LRC} = \int_{r_c}^{\infty} dr \int_0^{2\pi} d\phi u(r) r^2 \rho(R_i + r\sin\phi) \tag{C5}$$

Thus, the LRC energy of the kth element can be written as

$$u_{LRC}(R_k) = \sum_{i=1}^{N} H(R_{ik}) u_{i,LRC} \tag{C6}$$

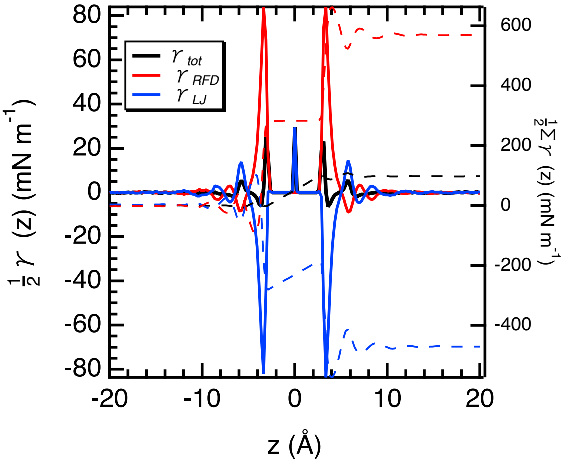

Figure D1. Local interfacial tensions of water molecules interacting with a graphene monolayer calculated with RFD and a cutoff radius of 12 Å. The profiles of the LJ and electrostatic parts are represented for comparison. The interfacial tensions are read on the right axis.

Appendix D. Contributions of Lennard-Jones and electrostatic contributions to the interfacial tension

References

[1] F. Goujon, P. Malfreyt, A. Boutin and A.H. Fuchs, Mol. Simul. **27**, 99–114 (2001).

[2] A. Ghoufi and P. Malfreyt, Mol. Phys. **104**, 2929–2943 (2006).

[3] A. Ghoufi, F. Goujon, V. Lachet and P. Malfreyt, J. Chem. Phys. **128**, 154718 (2008).

[4] N. Ferrando, V. Lachet, J. Pérez-Pellitero, A.D. Mackie, P. Malfreyt and A. Boutin, J. Phys. Chem. B **115**, 10654–10664 (2011).

[5] A. Ghoufi and P. Malfreyt, J. Chem. Phys. **136**, 024104 (2012).

[6] X. Paredes, J. Fernandez, A.A.H. Padua, P. Malfreyt, F. Malberg, B. Kirchner and A.S. Pensado, J. Phys. Chem. B **118**, 731–742 (2014).

[7] A. Ghoufi, P. Malfreyt and D.J. Tildesley, Chem. Soc. Rev. **45**, 1387–1409 (2016).

[8] P. Orea, J. Lopez-Lemus and J. Alejandre, J. Chem. Phys. **123**, 114702 (2005).

[9] J.R. Errington and D.A. Kofke, J. Chem. Phys. **127**, 174709 (2007).

[10] F. Biscay, A. Ghoufi, F. Goujon, V. Lachet and P. Malfreyt, J. Chem. Phys. **130**, 184710 (2009).

[11] F. Goujon, A. Ghoufi, P. Malfreyt and D.J. Tildesley, J. Chem. Theory Comput. **11**, 4575–4585 (2015).

[12] M. Guo and B. Lu, J. Chem. Phys. **106**, 3688–3695 (1997).

[13] J. Janeček, J. Chem. Phys. **131**, 6264–6269 (2006).

[14] J.M. Míguez, D.G. Salgado, J.L. Legido and M. Piñeiro, J. Chem. Phys. **132**, 184102 (2010).

[15] L.G. MacDowell and F. Blas, J. Chem. Phys. **131**, 074705–074714 (2009).

[16] J.G. Kirkwood and F.P. Buff, J. Chem. Phys. **17**, 338–343 (1949).

[17] J.H. Irving and J. Kirkwood, J. Chem. Phys. **18**, 817–829 (1950).

[18] F. Goujon, P. Malfreyt and D.J. Tildesley, Soft Matter **6**, 3472–3481 (2010).

[19] G. Maurel, F. Goujon, B. Schnell and P. Malfreyt, J. Phys. Chem. C **119**, 4817–4826 (2015).

[20] T. Dreher, C. Lemarchand, L. Soulard, E. Bourasseau, P. Malfreyt and N. Pineau, J. Chem. Phys. **148**, 034702 (2018).

[21] T. Dreher, C. Lemarchand, N. Pineau, E. Bourasseau, A. Ghoufi and P. Malfreyt, J. Chem Phys. **150**, 014703 (2019).

[22] T. Dreher, N. Pineau, E. Bourasseau, P. Malfreyt, L. Soulard and C. Lemarchand, J. Chem Phys. **151**, 244703 (2019).

[23] H.D. d'Oliveira, X. Davoy, E. Arche, P. Malfreyt and A. Ghoufi, J. Chem. Phys **146**, 214112 (2017).

[24] J.U. Lee, D. Yoon and H. Cheong, Nano Lett. **12**, 4444–4448 (2012).

[25] C.D. van Engers, N.E.A. Cousens, V. Babenko, J. Britton, B. Zappone, N. Grobert and S. Perkin, Nano Lett. **17**, 3815–3821 (2017).

[26] M.P. Allen and D.J. Tildesley, *Computer Simulation of Liquids*, 2nd ed. (Clarendon Press, Oxford, 2017).

[27] J. Alejandre, D.J. Tildesley and G.A. Chapela, Mol. Phys. **85**, 651–663 (1995).

[28] M. Neumann, J. Chem. Phys. **82**, 5663–5672 (1985).

[29] C.J. Fennell and J.D. Gezelter, J. Chem. Phys **124**, 234104 (2006).

[30] D.M. Heyes, Phys. rev. B **49**, 755–764 (1994).

[31] P.H. Hünenberger and W.F. van Gunsteren, J. Chem. Phys **108**, 6117 (1998).

[32] G. Mathias, B. Egwolf, M. Nonella and P. Tavan, J. Chem. Phys **118**, 10847 (2003).

[33] M.C. Gordillo and J. Marti, Phys. rev. B **78**, 075432 (2008).

[34] A. Akaishi, T. Yonemaru and J. Nakamura, ACS Omega **2**, 2184–2190 (2017).

[35] T.A. Ho and A. Strioloa, J. Chem. Phys. **138**, 054117 (2013).

[36] R.P. Misra and D. Blankschtein, J. Phys. Chem. C **121**, 28166–28179 (2017).

[37] J.C. Neyt, A. Wender, V. Lachet and P. Malfreyt, J. Phys. Chem. B **115**, 9421–9430 (2011).

[38] J.L.F. Abascal and C. Vega, J. Chem Phys. **123**, 234505 (2005).

[39] D. Cohen-Tanugi and J.C. Grossman, Nano Lett. **12**, 3602–3608 (2012).

[40] J. Alejandre, D.J. Tildesley and G.A. Chapela, J. Chem. Phys. **102**, 4574–4583 (1995).

[41] J.M. Míguez, M.M. Piñeiro and F.J. Blas, J. Chem. Phys. **138**, 34707–34716 (2013).

[42] I. Todorov and W.S. and, J. Mater. Chem. **16**, 1911–1918 (2006).

[43] S. Melchionna, G. Ciccotti and B.L. Holian, Mol. Phys. **78**, 533–544 (1993).

[44] G.J. Gloor, G. Jackson, F.J. Blas and E. de Miguel, J. Chem. Phys. **123**, 134703–134721 (2005).

[45] A. Ghoufi and P. Malfreyt, Phys. Chem. Chem. Phys **12**, 5203–5205 (2010).

[46] J. Rafiee, X. Mi, H. Gullapalli, A.V. Thomas, F. Yavari, Y. Shi, P.M. Ajayan and N.A. Koratkar, Nat. Mat. **11**, 217–222 (2012).

[47] F. Goujon, B. Bêche, P. Malfreyt and A. Ghoufi, J. Chem. Phys. **148**, 094702 (2018).

[48] R. Renou, A. Szymczyk, G. Maurin, P. Malfreyt and A. Ghoufi, J. Chem. Phys **142**, 184706 (2015).

[49] G.V. Lau, I.J. Ford, P.A. Hunt, E.A. Müller and G. Jackson, J. Chem. Phys. **142**, 114701 (2015).

[50] C. Ibergay, A. Ghoufi, F. Goujon, P. Ungerer, A. Boutin, B. Rousseau and P. Malfreyt, Phys. Rev. E **75**, 051602 (2007).